Journal of Magnetic Resonance **144,** 266–279 (2000)
doi:10.1006/jmre.2000.2042, available online at http://www.idealibrary.com on IDEAL®

Determination of Molecular Geometry by High-Order Multiple-Quantum Evolution in Solid-State NMR

Mattias Edén,*[,1] Andreas Brinkmann,* Henrik Luthman,* Lars Eriksson,† and Malcolm H. Levitt*[,2]

*Physical Chemistry Division, and †Structural Chemistry Division, Arrhenius Laboratory, Stockholm University, S-106 91 Stockholm, Sweden

Received October 8, 1999; revised February 3, 2000

The principles of molecular geometry determination by high-quantum heteronuclear local field spectroscopy in solid-state NMR are discussed. The extreme multiple-quantum coherences in a cluster of nuclear spins are allowed to evolve in the presence of heteronuclear through-space couplings to two spins of a different type. The multiple-quantum dephasing curve is independent of the homonuclear spin–spin couplings and may be described in terms of geometric parameters. The triple-quantum version of the experiment is demonstrated by determining the ψ torsion angle in a [$^{15}N_2$, $^{13}C_3$]-labeled sample of the peptide ala–ala–gly. Two regions of torsion angle space fit the experimental data, one in the neighborhood of −152° and one in the neighborhood of +161°. The latter determination is in excellent agreement with the X-ray estimate of +160.5°.

1. INTRODUCTION

Solid-state NMR is becoming an established tool for molecular structural determination in a wide variety of systems. Techniques have been introduced that allow accurate estimations of intermolecular distances (*1, 2*), as well as bond angles and torsional angles (*3–9*). Unlike solution NMR or X-ray diffraction, solid-state NMR is able to study large disordered molecular systems, such as polymers (*10*) and noncrystalline proteins (*11, 12*).

In solid-state NMR, molecular structural information is often obtained by studying the spin dynamics of clusters of magnetic nuclear spins, usually introduced by isotopic labeling at the sites of interest. In this paper, we consider heteronuclear spin clusters of the form S_MK_2, i.e., M spins of type S, located close in space to two spins of a different type K. Both species are assumed to be spin-$\frac{1}{2}$. The general aim is to design solid-state NMR experiments which locate the two K spins with respect to the cluster S_M, using only through-space dipolar coupling information.

Some specific cluster topologies are shown in Fig. 1. The first example (Fig. 1a) shows a S_2K_2 cluster. If the neighboring atoms are directly bonded, and if the bond lengths and bond angles are fixed, then the geometry of this unit is defined by the K_1–S_1–S_2–K_2 torsion angle. Double-quantum experiments for estimating torsion angles in this topology have been demonstrated (*6–8*). These experiments are only sensitive to the absolute magnitude of the torsion angle.

Figure 1b shows a S_3K_2 cluster. As shown below, excitation of triple-quantum coherence (3QC) in the S_3 unit allows the K_1–S_1–S_2–K_2 torsion angle to be estimated. If the four atoms S_1, S_2, S_3, and K_2 do not lie in the same plane, then 3Q experiments in the S_3K_2 system are sensitive to the sign of the K_1–S_1–S_2–K_2 torsion angle.

Figures 1c and 1d show more complex cluster topologies. In Fig. 1c, two torsion angles are necessary to define the geometry. In Fig. 1d, we consider a general case in which two K spins are in the vicinity of a S-spin cluster without being directly bound. The K spins are considered to be relatively distant (hence the dashed lines). For example, the cluster of S spins could be located in a labeled ligand, near the active site of a protein labeled with K spins. We anticipate that the experimental strategy discussed in this article may be adapted to the problem of locating and orienting a S-spin cluster with respect to two or more "triangulation points" (K spins), possibly located on a different molecule. Related experiments have been performed by the group of Schaefer, who have shown that REDOR distance estimates may be enhanced using multiple-quantum coherence (*13*). Distance measurements using REDOR variants have also been performed systems in which one S spin is coupled to several K spins (*13, 14*).

In principle, it is possible to extract geometrical information from the single quantum S-spin spectrum of the S_MK_2 systems. However, the single-quantum spin dynamics of such clusters is generally very complicated due to the large number of interactions. The evolution of the single-quantum coherences is normally dominated by the S-spin CSA interactions and the S–S through-space dipolar couplings. It is particularly difficult to extract the geometrical information in the presence of magic-angle-spinning, which provides good sensitivity and resolution, but which strongly attenuates the effect of the dipole–dipole couplings.

A great simplification of the spin dynamics may be achieved by incorporating as many S-spins as possible in a state of multiple-quantum coherence (MQC) (*15*). The simplest dynamical behavior is obtained for the extreme S-spin coherence

[1] Present address: Department of Chemistry, University of Illinois at Chicago, Chicago, IL 60607.

[2] To whom correspondence should be addressed. E-mail: mhl@physc.su.se.

1090-7807/00 $35.00

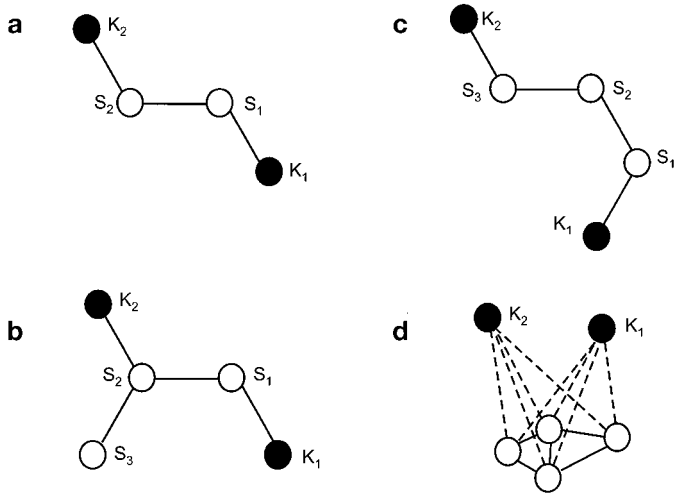

FIG. 1. Examples of heteronuclear spin systems of type S_MK_2 with different topologies. (a) S_2K_2. Evolution of S-spin double-quantum coherences under the four heteronuclear S–K couplings provides a direct measurement of the K_1–S_1–S_2–K_2 torsion angle. (b) One variant of the S_3K_2 model system: In this case, evolution of 3QC under the six S–K couplings gives information about the K_1–S_1–S_2–K_2 torsion angle. (c) Another S_3K_2 system: evolution of the 3Q S-spin coherence is sensitive to the relative orientation of the S_1K_1 and S_3K_2 vectors. Panel (d) shows a general S_MK_2 system, with distant K spins.

orders $\pm M$. If the K spins are spin-$\frac{1}{2}$, there are eight coherences of this type in S_MK_2 systems. The evolution of these coherences is independent of the S–S dipolar and J interactions. If other interactions, such as the K–K couplings and S-spin chemical shifts, are ignored or suppressed, then the extreme S-spin coherences evolve solely under the heteronuclear S–K dipolar interactions (*15*). The evolution of MQC is sensitive to the relative orientations of the heteronuclear dipolar couplings, and thereby provides a route for the direct determination of geometrical parameters. The dynamics may be described by simple formulas, even for large spin systems.

Experiments employing high-order MQC require reliable excitation techniques for the coherences. In systems of coupled spins-$\frac{1}{2}$, multiple-quantum excitation usually exploits the through-space S–S dipolar couplings. In static solids and liquid crystals, numerous demonstrations of high-order multiple-quantum excitation in systems of coupled spins-$\frac{1}{2}$ have been performed. Most experiments have involved strongly magnetic nuclei, such as ^{1}H (*16–22*) and ^{19}F (*23*), but demonstrations have also been performed on systems involving the nuclei ^{13}C (*24*) and ^{31}P (*25*).

In order to increase the sensitivity and spectral resolution, solid-state NMR studies of nonoriented samples are usually performed under magic-angle-spinning conditions. However, the rapid sample rotation has the disadvantage of suppressing the effect of the dipolar interactions which makes it more difficult to excite high-order MQC. For the type of experiments addressed here, these couplings need to be reintroduced. This applies to both the homonuclear S–S interactions that are required for *excitation* of the MQC, as well as the heteronuclear S–K couplings under which the coherences are allowed to *evolve*. Several techniques have been introduced for this purpose, both for recoupling of homonuclear and heteronuclear interactions (*26, 27*).

The spin-$\frac{1}{2}$ isotopes ^{13}C and ^{15}N are particularly interesting for biomolecular structural studies, since carbon and nitrogen nuclei compose the backbone structure of peptides and proteins. In what follows, we identify $S \equiv {}^{13}$C and $K \equiv {}^{15}$N. Carbon-13 double-quantum coherences in MAS NMR have been excited and exploited in numerous structural investigations (*6–8, 12, 27, 28*). Recently, we have also demonstrated that it is possible to excite ^{13}C triple-quantum coherences (*29*) under MAS conditions. High-order excitation of ^{1}H MQC in MAS on solids has also been demonstrated (*16, 19–22*).

The basic strategy of the present experiments is to excite the extreme ^{13}C coherences in a cluster of coupled ^{13}C spins, and then to let the coherences evolve under the recoupled ^{13}C–^{15}N dipolar interactions, independent of the homonuclear couplings and the chemical shifts (both isotropic and anisotropic). This class of experiments is demonstrated by estimating the peptide torsion angle ψ in a molecular fragment of the isotopically labeled tripeptide [^{15}N,$^{13}C_3$–ala]–[^{15}N–gly]–gly (AGG), which has the X-ray structure depicted in Fig. 2a. The cluster of three ^{13}C spins and two ^{15}N spins has the topology shown in Fig. 2b. The experiment is performed by exciting ^{13}C triple-quantum coherences (3QC) in the ^{13}C-labeled alanine residue. This experiment is referred to as NCCN-triple-quantum heteronuclear local field spectroscopy (NCCN-3Q-HLF). The torsion angle resolution of the method is about 5°, and it is possible to discriminate between positive and negative torsion angles. As shown below, the triple-quantum experiment complements existing techniques employing double-quantum coherence for estimation of torsion angles (*7, 8*).

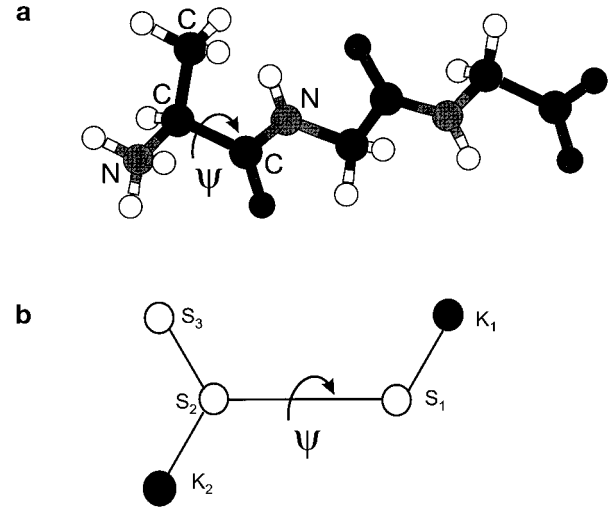

FIG. 2. (a) Molecular structure of ala–gly–gly monohydrate. The torsion angle ψ measured in the NCCN-3Q-HLF experiment is shown. (b) The coupling topology corresponding to the S_3K_2 spin cluster.

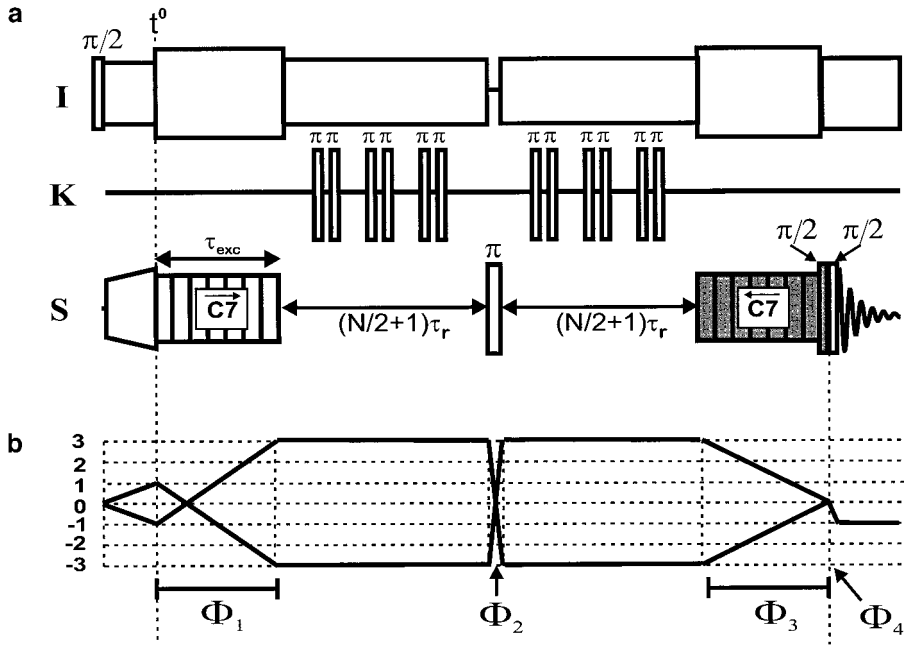

FIG. 3. (a) NCCN-3Q-HLF radio-frequency pulse scheme. (b) *S*-spin coherence transfer pathways during the experiment, as selected by the phase cycling scheme (see text).

2. THE NCCN-3Q-HLF EXPERIMENT

The NCCN-3Q-HLF experiment for measuring the torsion angle ψ in a [$^{15}N_2$, $^{13}C_3$]-labeled molecular fragment employs the pulse scheme shown in Fig. 3. This is a triple-resonance experiment, and starts with transfer of magnetization from ^{1}H (denoted *I*) to the ^{13}C (denoted *S*) by ramped cross-polarization (*30*). High-power unmodulated ^{1}H decoupling is applied for the rest of the pulse sequence (except for during the ^{13}C π-pulse).

The POST-*C*7 sequence (*31*), here denoted $\overrightarrow{C7}$, is applied to cross-polarized transverse magnetization in order to excite triple-quantum coherence (3QC) (*29*). The recoupled 2Q Hamiltonian generated by C7 partly converts the cross-polarized $\pm$1Q coherences into $\pm$3Q coherences. The 3QC is allowed to evolve in the presence of a series of π-pulses applied to the *K* spins, in order to recouple the heteronuclear *S*–*K* couplings (*2*). The 3QC is reconverted back into observable transverse magnetization by applying a modified POST-C7-sequence, denoted $\overleftarrow{C7}$, as described below. The signal is filtered through longitudinal magnetization by a pair of phase-shifted π/2-pulses, and the NMR signal is observed in the subsequent detection interval.

2.1. Excitation and Reconversion of Multiple Quantum Coherence

The C7 sequence (*31, 32*) consists of a set of rf cycles, each with an overall phase shift $\phi_p = \Phi + 2\pi\nu p/7$, where $p = 0, 1, 2, \ldots$, is the cycle index, and Φ is the starting phase. The "winding number" (*33, 34*) ν is given by $\nu = +1$ for $\overrightarrow{C7}$ and $\nu = -1$ for $\overleftarrow{C7}$. The use of opposite winding numbers is required by the change in double-quantum phases induced by the π pulse on the *S* spins in the middle of the evolution interval (*35*). Each cycle spans $\frac{2}{7}$ of a rotational period $\tau_r = |2\pi/\omega_r|$, where ω_r is the rotational frequency. In the POST-C7 implementation (*31*), the cycle used for excitation of 3QC corresponds to $\overrightarrow{C}_\phi = (\pi/2)_\phi(2\pi)_{\phi+\pi}(3\pi/2)_\phi$, and that for MQ reconversion to $\overleftarrow{C}_\phi = (3\pi/2)_\phi(2\pi)_{\phi+\pi}(\pi/2)_\phi$. We have found empirically that this choice of pulse sequence elements leads to improved overall efficiency, in this context. This behavior is not fully understood at present, but it is presumably due to cancellation of undesirable high-order terms. The two excitation and reconversion blocks of C7 are of equal duration $\tau_{\text{exc}} = \tau_{\text{reconv}}$. The starting phases of the excitation and reconversion blocks are denoted Φ_1 and Φ_3, respectively. These phases depend in a complicated way on the phase cycle and on the value of the evolution interval, specified fully below.

The excitation and reconversion scheme shown in Fig. 3 is suitable when exploiting odd-order multiple-quantum coherence in systems with an odd number of *S* spins. For systems with even numbers of *S* spins, even-quantum coherences are excited by inserting a π/2 pulse after the cross-polarization interval, and by removing one of the π/2 pulses at the end of the reconversion sequence. Note, however, that $\pm$4QC cannot be excited in four-spin-$\frac{1}{2}$ systems this way (*17, 18, 36, 37*).

2.2. Evolution of MQC

The MQC evolution interval between the two blocks of C7 irradiation has a duration equal to $N + 2$ rotational periods

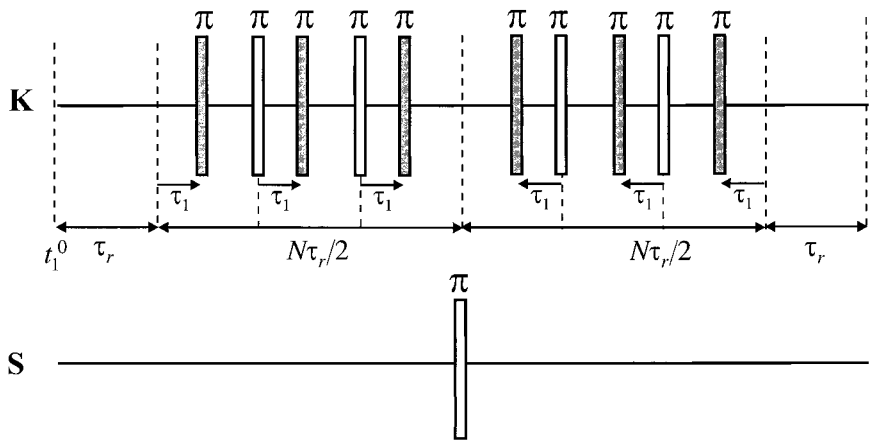

FIG. 4. Expansion of the central region in Fig. 3, showing the positions of the *K*-spin π-pulses for $\tau_1 \neq 0$ and $N = 6$. The positions of the shaded pulses depend on the parameter τ_1.

(Fig. 4). This interval contains $(2N - 2)$ π pulses applied to the *K* spins and one π pulse applied to the *S* spins. The positions of the *K*-spin pulses depend on the values of the evolution interval τ_1. A set of experiments is conducted with different values of τ_1. The arrangement of pulses corresponding to one particular evolution time τ_1 is depicted in Fig. 4. In general, the *p*th *K*-spin π-pulse is centered around the time-point t_p, specified by

$$\begin{aligned}
t_1 &= t_1^0 + \tau_r + \tau_1 \\
t_2 &= t_1^0 + 2\tau_r \\
t_3 &= t_1^0 + 2\tau_r + \tau_1 \\
t_4 &= t_1^0 + 3\tau_r \\
&\vdots \quad\quad \vdots \\
t_{N-2} &= t_1^0 + \frac{N}{2}\tau_r \\
t_{N-1} &= t_1^0 + \frac{N}{2}\tau_r + \tau_1 \\
t_N &= t_1^0 + \left(\frac{N}{2} + 2\right)\tau_r - \tau_1 \\
t_{N+1} &= t_1^0 + \left(\frac{N}{2} + 2\right)\tau_r \\
&\vdots \quad\quad \vdots \\
t_{2N-4} &= t_1^0 + N\tau_r - \tau_1 \\
t_{2N-3} &= t_1^0 + N\tau_r \\
t_{2N-2} &= t_1^0 + (N+1)\tau_r - \tau_1 ,
\end{aligned} \qquad [1]$$

where the time point t_1^0 indicates the start of the evolution interval as indicated in Fig. 4. A π-pulse is applied on the *S* channel at the time-point $t_1^0 + (N + 1)\tau_r/2$. The phase of this pulse is denoted Φ_2 (Fig. 3). This pulse refocuses evolution under isotropic chemical shifts during the evolution time period, as well as Bloch–Siegert shifts of the *S*-spin Larmor frequency during the *K*-spin pulses (*2, 35*). Since the overall evolution interval has a fixed duration equal to an even number of rotor periods, the evolution under the *S*-spin chemical shift anisotropy is suppressed.

Half of the *K*-spin π-pulses remain fixed, and the other half move toward the center of the evolution interval as τ_1 is increased. This pulse sequence strategy has been used before in the context of the REDOR experiment (*2*). There are other possibilities for recoupling the *S–K* interactions (*8, 38*).

In practice, the choice of *N* is dictated by the need to achieve sufficient heteronuclear modulation without too high relaxation losses. The experimental results discussed below employed $N = 8$ and the spinning frequency 5000 Hz.

In order to reduce the effect of pulse imperfections, we employed the following repeating sequence of rf phases {0, π/2, 0, π/2, π/2, 0, π/2, 0} for the *K*-spin π-pulses, as recommended in Ref. (*39*).

2.3. Z filter

We improved the phase properties of the triple-quantum filtered signals by employing a "*z*-filter" (*40*) prior to signal detection. This is done by two π/2 pulses of phases Φ_3 and Φ_4 (Fig. 3). The phases are varied in a phase cycling scheme (see below). The *z* filter selectively detects NMR signals passing through longitudinal magnetization and removes dispersive components of the spectral peaks.

2.4. Phase Cycling

The *S*-spin coherence transfer pathway of the experiment is shown in Fig. 3b. The indicated coherence transfer pathways are selected by adjusting the post digitization phase Φ_{dig} to satisfy the equation

$$\begin{aligned}
\Phi_{\text{dig}} = 3(\Phi_1 - \Phi_1^0) - 6(\Phi_2 - \Phi_2^0) + 3(\Phi_3 - \Phi_3^0) \\
- (\Phi_4 - \Phi_4^0) + \Phi_{\text{rec}},
\end{aligned} \qquad [2]$$

where Φ_{rec} is the rf receiver phase, and the pulse sequence blocks are cycled according to

$$\Phi_1 = \Phi_1^0 \quad [3a]$$

$$\Phi_2 = \Phi_2^0 + \frac{2\pi}{n_2}\,\mathrm{floor}\left\{\frac{\mathsf{m}}{n_3 n_4}\right\} \quad [3b]$$

$$\Phi_3 = \Phi_3^0 + 2\pi\mathsf{m}/n_3 \quad [3c]$$

$$\Phi_4 = \Phi_4^0 + \frac{2\pi}{n_4}\,\mathrm{floor}\left\{\frac{\mathsf{m}}{n_3}\right\} \quad [3d]$$

$$\Phi_{rec} = 0, \quad [3e]$$

where m is the transient counter $\mathsf{m} = 0, 1, 2, \ldots, 143$. The function floor($x$) returns the largest integer not greater than x. The initial phases were $\Phi_1^0 = \Phi_2^0 = 0$, $\Phi_3^0 = -\omega_r\tau_{exc}$, $\Phi_4^0 = 3\pi/2$. Note that the phase of the reconversion block Φ_3 depends on the duration of the excitation block, in order to achieve a correct phase correspondence between the average Hamiltonians in the multiple-quantum excitation and reconversion intervals (*32*). Our experiment employed $n_2 = 12$, $n_3 = 6$, and $n_4 = 2$, giving a total phase cycle comprising 144 steps. The values of n_1, n_2, n_3, and n_4 are dictated by the need to select both ± 3Q pathways in Fig. 3, according to the usual rules for phase cycling (*40*).

3. THEORY

3.1. Spin Hamiltonian

Consider a $S_M K_2$ spin system. We label the two K spins j and k and neglect the interactions with the abundant I spins (^{1}H), since high-power proton decoupling is performed throughout the experiment.

The high-field spin Hamiltonian at time-point t, in the absence of rf fields, may be expressed

$$H(t) = H_S(t) + H_K(t) + H_{SK}(t) + H_{SS}(t) \quad [4]$$

with

$$H_{SK}(t) = \sum_{n=1}^{M} \{\omega_{nj}^{SK}(t) + \pi J_{nj}^{SK}\} 2S_{nz}K_{jz} + \{\omega_{nk}^{SK}(t) + \pi J_{nk}^{SK}\} 2S_{nz}K_{kz} \quad [5]$$

$$H_{SS}(t) = \sum_{m,n=1}^{M} \omega_{mn}^{SS}(t)\,\frac{1}{2}\,(3S_{mz}S_{nz} - \mathrm{S}_m \cdot \mathrm{S}_n) + 2\pi J_{mn}^{SS}\mathrm{S}_m \cdot \mathrm{S}_n \quad [6]$$

$$H_S(t) = \sum_{n=1}^{M} \omega_n(t) S_{nz} \quad [7]$$

$$H_K(t) = \omega_j(t)\,K_{jz} + \omega_k(t)\,K_{kz}. \quad [8]$$

We ignore the homonuclear interactions between the K spins, since these are small in the case $K \equiv {}^{15}$N considered below. The heteronuclear and homonuclear J couplings are denoted J_{nj}^{SK} and J_{mn}^{SS}, respectively. The time-dependent heteronuclear (ω_{nj}^{SK}) and homonuclear (ω_{mn}^{SS}) dipolar couplings are given by

$$\omega_{nj}^{SK}(t) = b_{nj} \sum_{q',q=-2}^{2} D_{0q'}^{2}(\Omega_{\mathrm{PM}}^{nj})\, D_{q',q}^{2}(\Omega_{\mathrm{MR}})\, d_{q0}^{2}(\beta_{\mathrm{RL}}) \times \exp\{-\mathrm{i}q\alpha_{\mathrm{RL}}^{0}t\}\exp\{iq\omega_r t\}, \quad [9]$$

$$\omega_{mn}^{SK}(t) = b_{mn} \sum_{q',q=-2}^{2} D_{0q'}^{2}(\Omega_{\mathrm{PM}}^{mn})\, D_{q'q}^{2}(\Omega_{\mathrm{MR}})\, d_{q0}^{2}(\beta_{\mathrm{RL}}) \times \exp\{-\mathrm{i}q\alpha_{\mathrm{RL}}^{0}t\}\exp\{iq\omega_r t\}, \quad [10]$$

with b_{nj} and b_{mn} representing the dipole–dipole coupling constants defined by

$$b_{nj}^{SK} = -\frac{\mu_0}{4\pi}\,\gamma_S\gamma_K\hbar r_{nj}^{-3} \quad [11]$$

$$b_{mn}^{SS} = -\frac{\mu_0}{4\pi}\,\gamma_S^2\hbar r_{mn}^{-3}. \quad [12]$$

Here r_{jk} denotes the distance between nuclei j and k, and the other symbols have their usual meanings. The symbols $D_{q'q}^2$ and d_{q0}^2 represent second rank Wigner elements and reduced Wigner elements, respectively (*41*). $\Omega_{\mathrm{PM}}^{mn}$ denotes a set of Euler angles (*41*), specifying the transformation between the principal axis system of the coupling between spins m and n, and a frame of reference fixed on the molecule. Ω_{MR} specifies the transformation from this system to a frame fixed on the rotor. The angles Ω_{PM} are fixed by the molecular geometry, whereas the angles Ω_{MR} are random in a powder. The z axis of the rotor frame is along the sample rotation axis, which subtends an angle β_{RL} with respect to the static magnetic field direction. For magic-angle-spinning, $\beta_{\mathrm{RL}} = \arctan\sqrt{2}$. The angle α_{RL}^0 defines the position of the rotor at the time point $t = 0$.

Similar expressions hold for the chemical shift terms

$$\omega_m(t) = \omega_m^{\mathrm{iso}} + \sum_{q,q',q''=-2}^{2} [A_{2q''}^{m}]^P D_{q''q'}^{2}(\Omega_{\mathrm{PM}}^{m})\, D_{q'q}^{2}(\Omega_{\mathrm{MR}}) \times d_{q0}^{2}(\beta_{\mathrm{RL}})\exp\{-\mathrm{i}\alpha_{\mathrm{RL}}^{0}t\}\exp\{iq\omega_r t\}. \quad [13]$$

Here ω_m^{iso} is the isotropic chemical shift frequency of spin m

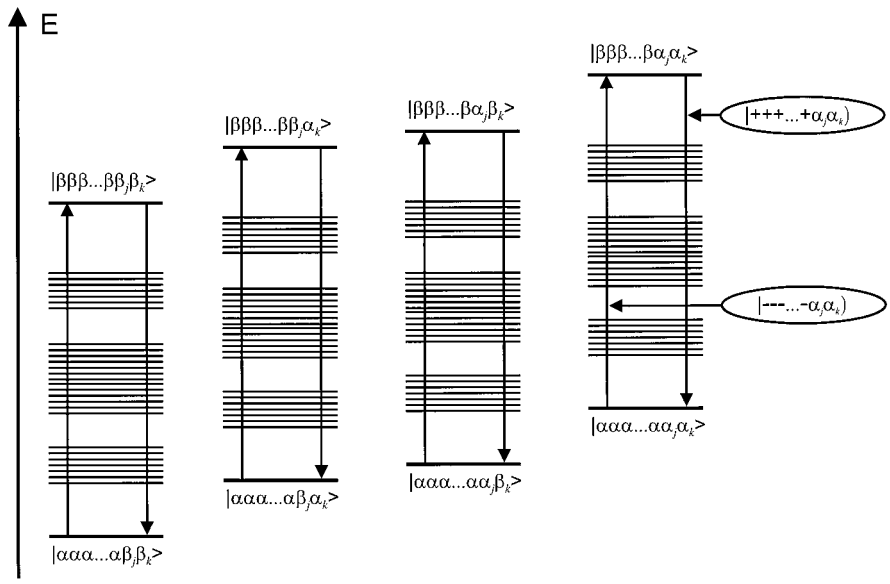

FIG. 5. Schematic energy levels for a $S_M K_2$ system, assuming $\gamma_S > 0$ and $\gamma_K < 0$ (as appropriate for the case $S = {}^{13}\mathrm{C}$ and $K = {}^{15}\mathrm{N}$). The eight extreme S-spin angular momentum states are labeled. The eight extreme S-spin multiple-quantum coherences are shown by arrows. Two such coherences are labeled explicitly.

and $[A^{m}_{2q''}]^{P}$ is the q''th component of the irreducible spherical tensor representing the chemical shift anisotropy, expressed in its principal axis system.

The rf Hamiltonian during pulses on either K or S spins is given by

$$H^{L}_{\mathrm{rf}}(t) = \omega^{L}_{\mathrm{nut}} \exp\{-\mathrm{i}\phi_p L_z\} L_x \exp\{\mathrm{i}\phi_p L_z\}; \quad L = K, S, \quad [14]$$

where $\omega^{L}_{\mathrm{nut}}$ is the nutation frequency, and ϕ_p is the phase of the pulse. The rf Hamiltonian is only finite during intervals $[t - \tau^{L}_{p}/2,\ t + \tau^{L}_{p}/2]$, where t is the center of the pulse. τ_p is the duration of the π-pulses, satisfying $\omega^{L}_{\mathrm{nut}}\tau_p = \pi$. In practice, the strong rf pulses also induce Bloch–Siegert shifts of the coherences associated with nonresonant spins, which have been observed to have a significant effect in REDOR experiments (*2*). However, the current experiments are compensated for these shifts, as discussed further in Ref. (*35*).

3.2. Multiple-Quantum Coherences

For a single spin-$\frac{1}{2}$ nuclei we denote the state with z component of spin angular momentum $m_j = \frac{1}{2}$ by $|\alpha\rangle$ and the state with $m_j = -\frac{1}{2}$ by $|\beta\rangle$. A convenient basis for describing the $S_M K_2$ spin system is constructed by taking direct products between the Zeeman states of the individual spins. A schematic picture of the energy levels of a $S_M K_2$ spin system (assuming positive magnetogyric ratio for S and negative magnetogyric ratio for K) is shown in Fig. 5. There are four states of the form $|\alpha\alpha\cdots\alpha m_j m_k\rangle$ and four states of the form $|\beta\beta\cdots\beta m_j m_k\rangle$ according to the quantum numbers m_j and m_k for the K spins, which are assumed to be spin-$\frac{1}{2}$.

$$|\alpha\alpha\cdots\alpha m_j m_k\rangle \equiv |\alpha_1\rangle \otimes |\alpha_2\rangle \otimes\cdots\otimes |\alpha_M\rangle \otimes |m_j\rangle \otimes |m_k\rangle \quad [15]$$

$$|\beta\beta\cdots\beta m_j m_k\rangle \equiv |\beta_1\rangle \otimes |\beta_2\rangle \otimes\cdots\otimes |\beta_M\rangle \otimes |m_j\rangle \otimes |m_k\rangle. \quad [16]$$

These states obey the eigenequations

$$S_z|\alpha\alpha\cdots\alpha m_j m_k\rangle = \frac{1}{2} M|\alpha\alpha\cdots\alpha m_j m_k\rangle \quad [17]$$

$$S_z|\beta\beta\cdots\beta m_j m_k\rangle = -\frac{1}{2} M|\beta\beta\cdots\beta m_j m_k\rangle \quad [18]$$

$$K_{jz}|\alpha\alpha\cdots\alpha m_j m_k\rangle = m_j|\alpha\alpha\cdots\alpha m_j m_k\rangle$$

$$K_{jz}|\beta\beta\cdots\beta m_j m_k = m_j|\beta\beta\cdots\beta m_j m_k\rangle \quad [19]$$

$$K_{kz}|\alpha\alpha\cdots\alpha m_j m_k\rangle = m_k|\alpha\alpha\cdots\alpha m_j m_k\rangle$$

$$K_{kz}|\beta\beta\cdots\beta m_j m_k = m_k|\beta\beta\cdots\beta m_j m_k\rangle, \quad [20]$$

where S_z is the operator for the z component of total S-spin angular momentum. The eight states $|\alpha\alpha\cdots\alpha m_j m_k\rangle$ and $|\beta\beta\cdots\beta m_j m_k\rangle$ are eigenstates of the high-field Hamiltonian and may therefore be used to label eight energy levels of the energy level diagram (Fig. 5).

In what follows, we use a Liouville space notation (*42*). The

operator for maximum positive order M of S-spin coherence, with K-spin quantum numbers m_j and m_k, is denoted

$$|+ + \cdots + m_j m_k) \equiv |\alpha\alpha \cdots \alpha m_j m_k\rangle\langle\beta\beta \cdots \beta m_j m_k|. \quad [21]$$

The operator for S spins having the extreme negative quantum coherence of order $-M$ is denoted

$$|- - \cdots - m_j m_k) \equiv |\beta\beta \cdots \beta m_j m_k\rangle\langle\alpha\alpha \cdots \alpha m_j m_k|. \quad [22]$$

Two of the eight $\pm M$-quantum coherences are denoted by arrows in Fig. 5. These are eigenoperators of the commutation superoperator for the total S-spin angular momentum $\hat{S}_z$

$$\hat{S}_z^{\text{comm}}|+ + \cdots + m_j m_k) = M|+ + \cdots + m_j m_k) \quad [23]$$

$$\hat{S}_z^{\text{comm}}|- - \cdots - m_j m_k) = -M|- - \cdots - m_j m_k), \quad [24]$$

where a commutator superoperator $\hat{A}^{\text{comm}}$ transforms a given operator B as follows (*42*):

$$\hat{A}^{\text{comm}}|B) = |[A, B]). \quad [25]$$

The eight extreme coherence operators are eigenoperators of the Hamiltonian commutator superoperator $\hat{H}^{\text{comm}}$:

$$\hat{H}^{\text{comm}}(t)|+ + \cdots + m_j m_k) = \{\omega_S^{\Sigma}(t) + \omega_{SK,J}^{m_j m_k} + \omega_{SK}^{m_j m_k}(t)\}|+ + \cdots + m_j m_k) \quad [26]$$

$$\hat{H}^{\text{comm}}(t)|- - \cdots - m_j m_k) = -\{\omega_S^{\Sigma}(t) + \omega_{SK,J}^{m_j m_k} + \omega_{SK}^{m_j m_k}(t)\}|- - \cdots - m_j m_k), \quad [27]$$

where $\omega_S^{\Sigma}(t)$, $\omega_{SK}^{m_j m_k}(t)$, and $\omega_{SK,J}^{m_j m_k}$ are sums of S-spin chemical shifts, heteronuclear throughspace dipolar, and J couplings, respectively:

$$\omega_S^{\Sigma}(t) = \sum_{n=1}^{M} \omega_n(t) \quad [28]$$

$$\omega_{SK}^{m_j m_k}(t) = 2 \sum_{n=1}^{M} (m_j \omega_{nj}^{SK}(t) + m_k \omega_{nk}^{SK}(t)) \quad [29]$$

$$\omega_{SK,J}^{m_j m_k}(t) = 2\pi \sum_{n=1}^{M} (m_j J_{nj}^{SK} + m_k J_{nk}^{SK}). \quad [30]$$

Note that the S–S couplings do not appear in the eigenfrequencies of the extreme $\pm M$-quantum coherences (*15*).

3.3. Evolution of Multiple Quantum Coherence

From the commutation relationships of Eqs. [26] and [27] we get the following equation for the evolution of the $\pm M$-quantum coherences over the interval $t_a \rightarrow t_b$ in the absence of rf pulses

$$\hat{U}^0(t_b, t_a)|+ + \cdots + m_j m_k) = \exp\{-i(\Phi_S^{\Sigma}(t_b, t_a) + \Phi_{SK}^{m_j m_k}(t_b, t_a) + \Phi_{SK,J}^{m_j m_k}(t_b, t_a))\}\ |+ + \cdots + m_j m_k), \quad [31]$$

and

$$\hat{U}^0(t_b, t_a)|- - \cdots - m_j m_k) = \exp\{+i(\Phi_S^{\Sigma}(t_b, t_a) + \Phi_{SK}^{m_j m_k}(t_b, t_a) + \Phi_{SK,J}^{m_j m_k}(t_b, t_a))\}\ |- - \cdots - m_j m_k), \quad [32]$$

with the definitions

$$\Phi_S^{\Sigma}(t_b, t_a) = \int_{t_a}^{t_b} \omega_S^{\Sigma}(t) dt, \quad [33]$$

$$\Phi_{SK}^{m_j m_k}(t_b, t_a) = \int_{t_a}^{t_b} \omega_{SK}^{m_j m_k}(t) dt \quad [34]$$

$$\Phi_{SK,J}^{m_j m_k}(t_b, t_a) = \omega_{SK,J}^{m_j m_k}(t_b - t_b). \quad [35]$$

The heteronuclear through-space dipolar couplings refocus over a full rotational period

$$\Phi_{SK}^{m_j m_k}(t_a + \tau_r, t_a) = 0. \quad [36]$$

The K-spin π-pulses prevent this process by implementing coherence transfer at suitably chosen time-points

$$\hat{R}_x^K(\pi)|+ + \cdots + m_j m_k) = |+ + \cdots + (-m_j)(-m_k)), \quad [37]$$

where the pulse propagation superoperator is

$$\hat{R}_x^K(\pi) = \exp\{-i\pi\hat{K}_x\}. \quad [38]$$

Similarly, the S-spin π-pulse performs the following coherence transfer

$$\hat{R}_x^S(\pi)|+ + \cdots + m_j m_k) = |- - \cdots - m_j m_k) \quad [39]$$

$$\hat{R}_x^S(\pi)|- - \cdots - m_j m_k) = |+ + \cdots + m_j m_k). \quad [40]$$

These relationships may be used to calculate the evolution of

the $\pm M$-quantum coherences over the pulse sequence segment specified in Fig. 3, in the case that relaxation is neglected

$$\hat{U}_{\text{evol}}(\tau_1)|+ + \cdots + m_j m_k) = \exp\{-\mathrm{i}\Phi_{\text{evol}}^{m_j m_k}(\tau_1)\}|- - \cdots - m_j m_k) \quad [41]$$

$$\hat{U}_{\text{evol}}(\tau_1)|- - \cdots - m_j m_k) = \exp\{+\mathrm{i}\Phi_{\text{evol}}^{m_j m_k}(\tau_1)\}|+ + \cdots + m_j m_k). \quad [42]$$

The phase $\Phi_{\text{evol}}^{m_j m_k}(\tau_1)$ may be derived to different degrees of approximation. Assuming infinitely strong π-pulses, ($\tau_p = 0$) gives the following expression for $\Phi_{\text{evol}}^{m_j m_k}(\tau_1)$:

$$\Phi_{\text{evol}}^{m_j m_k}(\tau_1) = N\{\Phi_{SK}^{m_j m_k}(\tau_1 + t_1^0,\, t_1^0) + \Phi_{SK}^{m_j m_k}(\tau_r - \tau_1 + t_1^0,\, t_1^0)\}. \quad [43]$$

If the finite pulse durations are taken into account, one obtains

$$\Phi_{\text{evol}}^{m_j m_k}(\tau_1) = \left(\frac{N}{2} - 1\right)\Phi_A^{m_j m_k} + \Phi_B^{m_j m_k}, \quad [44]$$

with

$$\begin{aligned}\Phi_A^{m_j m_k}(\tau_1) = {} & \Phi_{SK}^{m_j m_k}\left(\tau_r - \frac{1}{2}\tau_p^K + t_1^0,\, \tau_r - \tau_1 + \frac{1}{2}\tau_p^K + t_1^0\right) \\ & + \Phi_{SK}^{m_j m_k}\left(\tau_r - \frac{1}{2}\tau_p^K + t_1^0,\, \tau_1 + \frac{1}{2}\tau_p^K + t_1^0\right) \\ & - \Phi_{SK}^{m_j m_k}\left(\tau_r - \tau_1 - \frac{1}{2}\tau_p^K + t_1^0,\, \frac{1}{2}\tau_p^K + t_1^0\right) \\ & - \Phi_{SK}^{m_j m_k}\left(\tau_1 - \frac{1}{2}\tau_p^K + t_1^0,\, \frac{1}{2}\tau_p^K + t_1^0\right) \quad [45]\end{aligned}$$

$$\begin{aligned}\Phi_B^{m_j m_k}(\tau_1) = {} & \Phi_{SK}^{m_j m_k}\left(\tau_r + t_1^0,\, \tau_r - \tau_1 + \frac{1}{2}\tau_p^K + t_1^0\right) \\ & + \Phi_{SK}^{m_j m_k}\left(\tau_r - \frac{1}{2}\tau_p^S + t_1^0,\, \tau_1 + \frac{1}{2}\tau_p^K + t_1^0\right) \\ & - \Phi_{SK}^{m_j m_k}\left(\tau_r - \tau_1 - \frac{1}{2}\tau_p^K + t_1^0,\, \frac{1}{2}\tau_p^S + t_1^0\right) \\ & - \Phi_{SK}^{m_j m_k}\left(\tau_1 - \frac{1}{2}\tau_p^K + t_1^0,\, t_1^0\right). \quad [46]\end{aligned}$$

These expressions depend only on the heteronuclear dipolar couplings, and are independent of the homonuclear dipolar couplings. This is a consequence of using the extreme $\pm M$-quantum S-spin coherences. In some cases, it is possible to use lower quantum orders in combination with "constant-time evolution" to achieve a similar effect (*43*). However, the isolation of the heteronuclear spin–spin interactions is only approximate in that case.

The expressions in Eqs. [43]–[46] are independent of the S-spin chemical shifts, due to the refocusing effect of the S-spin π-pulse and the use of equal numbers of complete sample revolutions before and after this pulse. The extreme MQ coherences undergo a relatively simple evolution, which may be simulated using a rather small number of geometrical parameters and without any consideration of the S-spin chemical shift anisotropies or homonuclear couplings.

3.4. The Signal

The multiple-quantum filtered signal amplitude $a(\tau_1, \Omega_{\text{MR}})$ for a given orientation Ω_{MR} is given by

$$a(\tau_1, \Omega_{\text{MR}}) = \sum_{m_j, m_k} \frac{(S^-|\hat{U}^{\text{reconv}}\hat{P}_{m_j m_k}^{(-M)}\hat{U}_{\text{evol}}(\tau_1)\hat{P}_{m_j m_k}^{(+M)}\hat{U}^{\text{exc}}|S_x)}{(S_x|S_x)} + \frac{(S^-|\hat{U}^{\text{reconv}}\hat{P}_{m_j m_k}^{(+M)}\hat{U}_{\text{evol}}(\tau_1)\hat{P}_{m_j m_k}^{(-M)}\hat{U}^{\text{exc}}|S_x)}{(S_x|S_x)}. \quad [47]$$

Here $\hat{P}_{m_j m_k}^{(\mp M)}$ are the projection superoperators for S-spin MQC of order $\pm M$:

$$\hat{P}_{m_j m_k}^{(+M)} = \frac{|+ + \cdots + m_j m_k)(+ + \cdots + m_j m_k|}{(+ + \cdots + m_j m_k|+ + \cdots + m_j m_k)}, \quad [48]$$

$$\hat{P}_{m_j m_k}^{(-M)} = \frac{|- - \cdots - m_j m_k)(- - \cdots - m_j m_k|}{(- - \cdots - m_j m_k|- - \cdots - m_j m_k)}. \quad [49]$$

Equation [47] assumes that the density operator after the cross-polarization interval is proportional to S_x, and that S^- is the observable corresponding to a quadrature detected NMR signal. The projection superoperators take into account the phase cycling, which selects the coherence transfer pathways specified in Fig. 3b.

The expressions for the signal amplitude Eq. [47] may be expressed

$$a(\tau_1, \Omega_{\text{MR}}) = \sum_{m_j m_k} a_{m_j m_k}^{(+M)}(\tau_1, \Omega_{\text{MR}}) + a_{m_j m_k}^{(-M)}(\tau_1, \Omega_{\text{MR}}), \quad [50]$$

where $a_{m_j m_k}^{(+M)}(\tau_1, \Omega_{\text{MR}})$ is the contribution from an individual $(+M)$-quantum coherence given by

$$a_{m_j m_k}^{(+M)}(\tau_1, \Omega_{\text{MR}}) = \exp\{-\mathrm{i}\Phi_{\text{evol}}^{m_j m_k}\} \times \frac{(S^-|\hat{U}^{\text{reconv}}|+ + \cdots + m_j m_k)(- - \cdots - m_j m_k|\hat{U}^{\text{exc}}|S_x)}{(S_x|S_x)} \quad [51]$$

$$a^{(-M)}_{m_j m_k}(\tau_1, \Omega_{\mathrm{MR}})) = \exp\{-\mathrm{i}\Phi^{m_j m_k}_{\mathrm{evol}}\}$$

$$\times \frac{(S^-|\hat{U}^{\mathrm{reconv}}|- - \cdots - m_j m_k)(+ + \cdots + m_j m_k|\hat{U}^{\mathrm{exc}}|S_x)}{(S_x|S_x)} \quad [52]$$

The propagators for excitation and reconversion processes depend on the pulse sequence used. A large number of methods for multiple-quantum excitation exist (*26, 27*). In the pulse scheme shown in Fig. 3, C7 pulse sequences are used for the excitation and reconversion of the triple-quantum coherence. In this case, the excitation and reconversion propagators are given by

$$\hat{U}^{\mathrm{exc}} = \hat{U}^{\bar{C7}}(\tau_{\mathrm{exc}}) \quad [53a]$$

$$\hat{U}^{\mathrm{reconv}} = \hat{U}^{\bar{C7}}(\tau_{\mathrm{reconv}}), \quad [53b]$$

with the propagators for C7 given by

$$\hat{U}^{\bar{C7}}(\tau) = \exp\{-\mathrm{i}\tau\hat{\bar{H}}_{\bar{C7}}\} \quad [54a]$$

$$\hat{U}^{\bar{C7}}(\tau) = \exp\{-\mathrm{i}\tau\hat{\bar{H}}_{\bar{C7}}\}, \quad [54b]$$

and the corresponding effective Hamiltonians are (ignoring J couplings)

$$\bar{H}_{\bar{C7}} = \frac{1}{2}\sum_{j<k}|\omega^{C7}_{jk}|(S^+_j S^+_k \exp\{-\mathrm{i}\phi_{C7}\} + S^-_j S^-_k \exp\{\mathrm{i}\phi_{C7}\})\exp\{\mathrm{i}2\Phi_1\} \quad [55a]$$

$$\bar{H}_{\bar{C7}} = \frac{1}{2}\sum_{j<k}|\omega^{C7}_{jk}|(S^+_j S^+_k \exp\{\mathrm{i}\phi_{C7}\} + S^-_j S^-_k \exp\{-\mathrm{i}\phi_{C7}\})\exp\{\mathrm{i}2\Phi_3\}. \quad [55b]$$

The nutation frequency and phase of the effective double quantum field during C7 are

$$|\omega^{C7}_{jk}| = b_{jk}\frac{343\sqrt{6}}{780\pi}(1 + \sin\{\pi/14\})^{1/2} \times \sum_{m=-2}^{2} d^2_{0m}(\beta^{jk}_{\mathrm{PM}})d^2_{m-1}(\beta_{\mathrm{MR}}) \times \exp\{-\mathrm{i}m(\gamma^{jk}_{\mathrm{PM}} + \alpha_{\mathrm{MR}})\}, \quad [56]$$

and

$$\phi_{C7}(t^0) = -\arctan\left(\frac{1 + \sin(\pi/14)}{\cos(\pi/14)}\right) - \omega_r t^0 + \gamma_{\mathrm{MR}}, \quad [57]$$

respectively.

The signal $a(\tau_1, \Omega_{\mathrm{MR}})$ evaluates to

$$a(\tau_1, \Omega_{\mathrm{MR}}) = \frac{1}{2} f^{C7}_{MQ}(\tau_{\mathrm{exc}}, \Omega_{\mathrm{MR}}) \times (\cos\{\Phi^{\alpha\alpha}_{\mathrm{evol}}(\tau_1)\} + \cos\{\Phi^{\alpha\beta}_{\mathrm{evol}}(\tau_1)\}) \quad [58]$$

where $f^{C7}_{MQ}(\tau_{\mathrm{exc}}, \Omega_{\mathrm{MR}})$ includes the orientational dependence of the excitation and reconversion of MQC. In the case of triple-quantum excitation in S_3K_2-spin systems, the following analytical expression has been derived (*29*)

$$f^{C7}_{3Q}(\tau_{\mathrm{exc}}, \Omega_{\mathrm{MR}}) = \frac{|\omega_{jk}\omega_{jm} + \omega_{jk}\omega_{km} + \omega_{jm}\omega_{km}|^2}{27\omega^4_{\mathrm{rms}}} \times \sin^4\left(\frac{\sqrt{3}}{2}\omega_{\mathrm{rms}}\tau_{\mathrm{exc}}\right), \quad [59]$$

which applies to the case $\Phi_1 = 0$. The root-mean-square frequency is defined

$$\omega_{\mathrm{rms}} = \frac{1}{\sqrt{3}}(\omega_{jk}\omega^*_{jk} + \omega_{jm}\omega^*_{jm} + \omega_{km}\omega^*_{km})^{1/2}. \quad [60]$$

Note that these expressions only depend on the magnitude of the dipolar couplings and their relative orientations, i.e., the three-dimensional geometry of the spin system.

For a powdered sample, Eq. [58] must be integrated over all possible molecular orientations Ω_{MR}:

$$a(\tau_1) = \langle a(\tau_1, \Omega_{\mathrm{MR}})\rangle_{\Omega_{\mathrm{MR}}} = \frac{1}{8\pi^2}\int_0^{2\pi} d\alpha_{\mathrm{MR}} \int_0^{\pi} \sin\beta_{\mathrm{MR}}\, d\beta_{\mathrm{MR}} \int_0^{2\pi} d\gamma_{\mathrm{MR}}\, a(\tau_1, \Omega_{\mathrm{MR}}). \quad [61]$$

For $M > 2$, the powder average amplitudes $a(\tau_1)$ depend on the sign of the torsion angle ψ. This behavior is different from the case $M = 2$, where the amplitudes $a(\tau_1, \Omega_{\mathrm{MR}})$ for a *single* molecular orientation depend on the sign of ψ, but where the sign-dependence is removed by the powder average over all orientations Ω_{MR}. In the case of $M > 2$, the dependence on the sign of ψ persists, due to the nonsymmetrical configuration of the entire spin system. Note carefully that the dependence on the sign of ψ is *not* solely due to the change in the *magnitudes* of the long-range heteronuclear interactions. In the spin system of Fig. 2b, the *relative orientations* of the S_1–K_1 and S_3–K_2

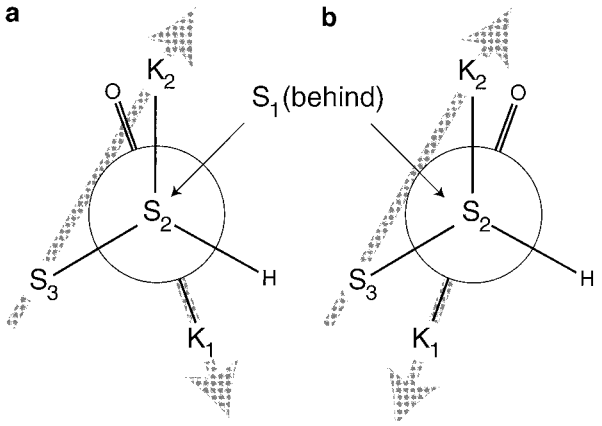

FIG. 6. Newman projections of the spin system in Fig. 2b, for the cases (a) $\psi = +160°$, and (b) $\psi = -160°$. The large arrows indicate the principal axes of the S_3–K_2 and the S_1–K_1 dipolar couplings. The relative orientation of these couplings is different for the two signs of the torsion angle. In addition, the S_3–K_1 distance is different in (a) and (b). In practice, both effects lead to a dependence of the 3Q evolution curve on the sign of ψ.

interactions are different for different signs of ψ, and this fact is sufficient to break the symmetry, without the participation of the weak S_3–K_1 interaction. This point is illustrated in Fig. 6, which shows Newman projections of the spin system in Fig. 2b, for the case $\psi = +160°$ and $\psi = -160°$. The large gray arrows indicate the directions of the S_3–K_2 and S_1–K_1 interaction terms. The relative orientation of the two tensors is quite different for the two signs of ψ. In addition, the magnitude of the long-range S_3–K_1 interaction depends on the sign of ψ. In practice, both effects contribute to break the symmetry with respect to sign inversion of ψ.

The pulse sequence shown in Fig. 3 is appropriate for systems with any *odd* order of coupled S spins. However, analytical solutions for the multiple-quantum excitation do not currently exist for $M > 3$. The multiple-quantum excitation dynamics may nevertheless be treated by numerical diagonalization of the average Hamiltonians in Eq. [55], or by explicit spin dynamical simulations using all spin interaction parameters.

In the case of even quantum excitation in systems of even numbers of spins, two additional $\pi/2$ pulses must be inserted in order to convert the cross-polarized transverse magnetization into z magnetization, and to convert the final z magnetization into observable signal. The propagators in the case of *even M* are therefore

$$\left.\begin{aligned}\hat{U}^{\text{exc}} &= \hat{U}^{\bar{C7}}\hat{R}_y^S(\pi/2)\\ \hat{U}^{\text{reconv}} &= \hat{R}_y^S(-\pi/2)\hat{U}^{\bar{C7}}\end{aligned}\right\} M \text{ even.} \qquad [62]$$

4. RESULTS

We have demonstrated the NCCN-3Q experiment by applying it to a crystalline sample of the isotopically labeled tripeptide [^{15}N, $^{13}C_3$–ala]–[^{15}N–gly]–gly (AGG), diluted in nonlabeled material (1:2). The sample is referred to as 33%-[$^{15}N_2$, $^{13}C_3$]-AGG.

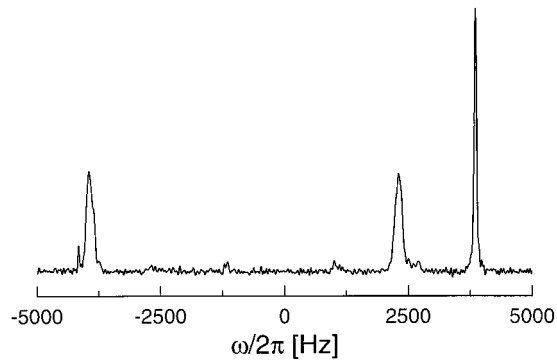

FIG. 7. CP-MAS ^{13}C spectrum of 33%-[$^{15}N_2$, $^{13}C_3$]-AGG at a spinning frequency of $\omega_r/2\pi = 5000$ Hz. The spectrum is the result of 24 transients.

Figure 7 shows the ^{13}C spectrum obtained from a standard cross-polarization experiment (the cross polarization interval was 1.00 ms), followed by signal acquisition. Figure 8 shows the triple-quantum filtered spectrum obtained using the pulse sequence in Fig. 3, using $\tau_1 = 0$, i.e., with no heteronuclear evolution of the 3QC. As discussed in Ref. (*29*), most of the spectral intensity is concentrated in the C^α peak. All spectral peaks in Fig. 8 are in pure absorption mode. This spectrum may be compared with that given in Fig. 2b of Ref. (*29*), which was obtained without employing the z filter. In that case, small dispersion amplitudes were obtained.

The experimental triple-quantum filtering efficiency was only around 2.5%. As discussed in Ref. (*29*), the theoretical maximum efficiency for 3Q filtering using this pulse scheme is around 6%. The remaining losses are due to relaxation, pulse imperfections, and insufficient proton decoupler power during the C7 sequences.

A set of integrated multiple-quantum filtered amplitudes for 15 values of τ_1 and $N = 8$ is shown in Fig. 9.

The peak amplitudes for each evolution time τ_1 were estimated as follows. A synthetic noiseless spectrum was generated, containing three Lorentzian weighting functions, whose

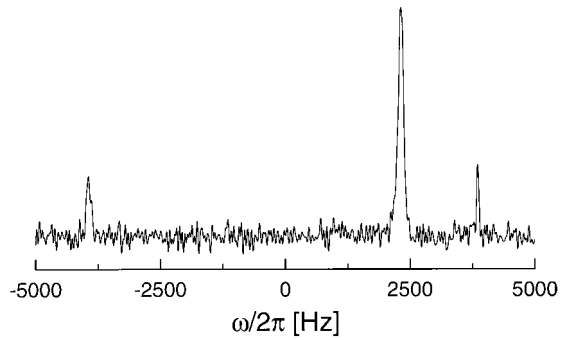

FIG. 8. 3QF ^{13}C spectrum of 33%-[$^{15}N_2$, $^{13}C_3$]-AGG from a NCCN-3Q-HLF experiment at $\omega_r/2\pi = 5000$ Hz. The spectrum is for $N = 8$ and $\tau_1 = 0$. The spectrum is the result of 2304 transients.

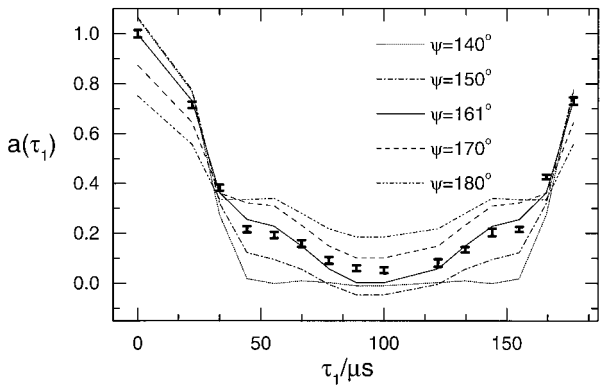

FIG. 9. Experimental 3Q-filtered amplitudes compared with a selection of calculated best-fit dephasing curves with positive values of ψ. The error bars represent the standard deviation of the noise.

widths and center frequencies matched the experimental peaks in the $\tau_1 = 0$ spectrum. The experimental spectra were multiplied by this masking function and integrated with respect to frequency. These integrals were identified as the experimental amplitudes. The same synthetic spectrum was used for all τ_1-increments. The standard deviation of the noise was estimated for each spectrum by using the same procedure, but shifting the Lorentzian masking functions so that they only covered signal-free regions. This procedure was repeated 1500 times, with random positions of the Lorentzian functions. The standard deviation of these 1500 integrals was used as an estimate of the noise variance for each experimental point (shown by error bars in Fig. 9). The noise variance was found to vary slightly, probably due to pulse breakthrough and other instabilities.

X-ray crystallography was performed on a single crystal of the AGG sample and the crystal structure was proved to be identical to that in Ref. (*44*).

The NMR simulations used the geometrical parameters (bond lengths and bond angles) from Ref. (*44*), with the exception of the torsion angle ψ, which was the only free geometrical parameter. Dephasing curves $a(\tau_1)$ were calculated as a function of ψ, and are shown in Fig. 9. The simulations included the calculated orientational dependence of the 3Q excitation as well as correction for finite pulse-durations (Eq. [44]). Assumptions made in the simulations are (i) isolated S_3K_2 spin systems during the experimental time-scale, (ii) neglect of the ^{15}N–^{15}N couplings (which are smaller than 60 Hz for all values of ψ), (iii) perfect performance of the π pulses, and (iv) negligible orientation dependence of the initial cross-polarization. A selection of best-fit calculated curves with positive values of ψ are plotted in Fig. 9, together with the experimental data. The noise variances are given as error bars for each spectrum.

Each of the calculated curves was fitted against the experimental data, by minimizing χ^2, according to

$$\chi^2 = \sum_h \frac{1}{\sigma_h^2} \{a_h^{\exp} - A a_h^{\text{calc}}\}^2, \qquad [63]$$

where $a_h^{\exp}$ and a_h^{calc} is the experimental and calculated value of $a(h\Delta\tau_1)$, respectively. σ_h is the standard deviation of the experimental noise, which was estimated independently for each τ_1-value. A represents an overall scaling factor by which the values of each simulated curve are multiplied. This together with the torsion angle are the only adjustable parameters.

In previous 2Q-HLF experiments (*7*, *8*), it was necessary to include an additional parameter for the decay of the 2QC over the variable evolution interval and a separate experiment for determination of this parameter. This is not necessary in the current implementation, since the total evolution interval does not depend on τ_1.

The experimental results are compared with best-fit simulations for a range of negative torsion angles in Fig. 10. In this case, $\psi = -152°$ provides the best fit. The quality of the fit for $\psi = -152°$ is approximately the same as the X-ray value for $\psi = +161°$. The torsion angle $\psi = -160°$ is clearly incompatible with the experimental results.

A plot of χ^2 for the experimental data and the best-fit simulations against ψ is shown in Fig. 11. This plot shows clearly the *two* minima in χ^2, one at $\psi = +161°$ and one at $\psi = -152°$. The lack of symmetry about $\psi = 0$ has been discussed above.

It should be noted that the simulations do not match the experimental measurements satisfactorily, given the measured noise variance. The minimum value of χ^2 is well above that which would be expected for a "good" fit. This does not degrade the quality of the torsion angle measurement significantly, but it is nevertheless a case for concern. Similar deviations have been observed in related experiments (*7*). At the moment, we do not understand the reason for these discrepancies, which are consistent and reproducible. Possible reasons could be minor asymmetric molecular vibrations, pulse imperfections, nonuniform cross-polarization, or minor spin interactions which are missing from the theoretical model. Intermo-

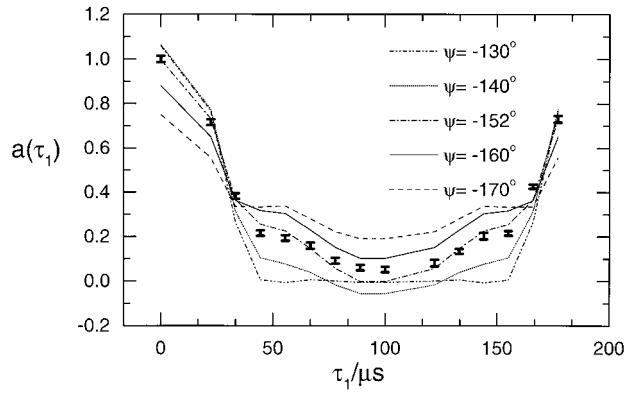

FIG. 10. As in Fig. 9, but with a selection of calculated best-fit dephasing curves with negative values of ψ.

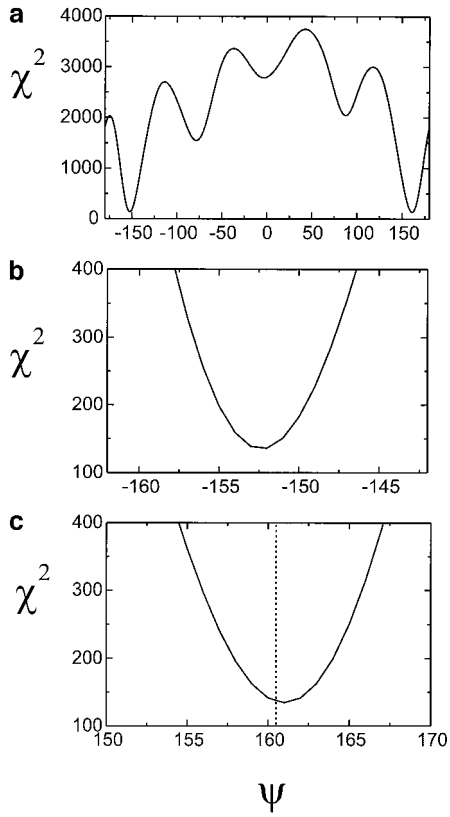

FIG. 11. χ^2 deviation between simulated and experimental data, plotted as a function of ψ over the following ranges: (a) $0° \le \psi \le 360°$, (b) $-142° \le \psi \le -162°$, (c) $150° \le \psi \le 170°$. The value of ψ obtained from a single-crystal X-ray study of the sample is shown (dashed line).

lecular couplings are unlikely to be the reason, since an experiment performed on a more dilute sample (1:9) displays similar discrepancies.

5. EXPERIMENTAL

The AGG sample was prepared by solid-state synthesis starting from N-α-Fmoc-alanine (98% $^{13}C_3$, 99% ^{15}N) and N-α-Fmoc-glycine (98% ^{15}N). The labeled tri-peptide was purified by HPLC and mixed with nonlabeled AGG (1:2). The mixed tripeptides were cocrystallized in water by slow evaporation of the solution. We verified by single-crystal X-ray diffraction that the crystal structure was identical to that given in Ref. (*44*).

All NMR experiments were performed at a magnetic field of 4.7 T on a Chemagnetics Infinity-200 spectrometer at a spinning frequency of $|\omega_r/2\pi| = 5000$ Hz. Approximately 50 mg of the sample was filled in a 4-mm zirconium oxide rotor. The NCCN-3Q-HLF experiment used $N = 8$ and an increment in τ_1 of 11.1 μs. The relaxation delay was 5 s. The durations of the ^{13}C and ^{15}N π-pulses were 7.3 and 8.0 μs, respectively, and the ^{13}C $\pi/2$-pulse was 3.5 μs. The duration of C7 excitation and reconversion intervals were 857.1 μs, corresponding to 15 *C* cycles. The experiment employed the following ^1H nutation frequencies: 83 kHz during acquisition; 109 kHz during C7; 100 kHz during the evolution interval (except during the ^{13}C pulse, when the decoupling was turned off).

Fifteen experiments with different τ_1 values were performed. In order to reduce the effects of long-term instrumental instabilities, the time signal was acquired in blocks that were added prior to processing. Each of the 15 signals was a sum of 2304 accumulated transients.

6. DISCUSSION

In this paper we have shown that it is possible to extend the existing double-quantum torsion angle experiments (*7, 8*) to higher orders of multiple quantum coherence. This allows geometry determinations on clusters of many spins, without compromising the simplicity of the mathematical description of the experiment. It is still possible to interpret the dephasing curves of the multiple-quantum coherences using only the geometrical parameters of the spin system (heteronuclear distances and angles), without taking chemical shift and *J* coupling terms into account. In the case of triple-quantum excitation in three-spin systems, closed formulas may be given for the curves as a function of molecular orientation.

In the case of the [$^{15}N_2$, $^{13}C_3$]-labeled AGG sample, a reasonable fit between experiment and simulation is obtained for the two angles $\psi = +161°$ and one at $\psi = -152°$. The first of these values corresponds well to the X-ray value ($\psi = +160.5°$). However, the geometry $\psi = -152°$ gives an equally good fit and cannot be excluded by this experiment alone.

Previous versions of the NCCN-HLF experiment employing 2QC (*7, 8*), estimate the *absolute value* of the torsional angle, leaving the sign undetermined. In the 3Q-HLF case, the presence of the third carbon atom breaks the symmetry of the phase functions, thus making it possible to distinguish between positive and negative values of ψ.

In principle it should be feasible to *uniquely* determine the value of ψ, including the sign, by combining information from an 2Q-HLF experiment with that obtained from an 3Q-HLF experiment. This currently requires molecules with two different types of carbon labeling, since the 2Q experiment cannot be applied directly to the $^{13}C_3$-labeled compound, due to the interference from *S–S* interactions, as discussed above. However, the use of two different samples might be avoided by employing a multidimensional extension of the 2Q experiment, in order to apply this to the $^{13}C_3$-labeled sample. This possibility is currently under investigation.

An interesting feature of Fig. 11a is that there is *no* value of ψ around which the χ^2 curve is symmetric. This indicates that the torsion angle might be estimated unambiguously in some molecules, using only the 3Q experiment.

Although the experiment described here has many interesting features, it would be problematic to use for large biomolecular systems, due to its low sensitivity. Clearly, new methodologies are needed for more efficient excitation of high order multiple quantum coherences in solids. Recent publications

indicate a renewed interest in high-order multiple quantum excitation (*19–22, 24, 29*).

The current experiment is limited to a spinning frequency of around 6 kHz, mainly due to the rf field requirements of the C7 sequences and the need to accomplish good proton decoupling while exciting the MQC. The REDOR sequences are also limited to relatively low spinning frequencies. In principle, the use of a rather low spinning frequency does not compromise the accuracy of the experiment, since the extreme multiple-quantum evolution is in any case unaffected by chemical shift anisotropies and homonuclear couplings. Nevertheless, the use of a low spinning frequency does degrade the available signal strength, since the chemical shift anisotropies and homonuclear couplings do cause modulations of the single-quantum coherences during detection. The technique could be readily adapted to high spinning frequency by replacing the C7 and REDOR recoupling sequences by variants which are designed to function under fast spinning (*8, 34, 38, 43*).

In its present form, the 3Q-NCCN experiment is experimentally demanding and provides very poor signal strength. Against these disadvantages should be weighed the advantage of relatively simple data analysis, employing a minimum of assumptions, and without the need for explicit spin dynamical simulations. There are few other techniques which are capable of comparable accuracy in the solid-state NMR of multiple-spin systems. One may compare, for example, with the selective rotational resonance experiments on a fully labelled amino acid (*45*). Quantitative geometrical information was only made available by demanding multiple-spin simulations including chemical shift anisotropies and many homonuclear couplings. Different approaches such as the CSA correlation methods of Tycko *et al.* (*5*), are currently limited to magnetically dilute spin pairs. It may be possible to extract torsion angle information from multiple-labeled samples using three-dimensional spectroscopy, but such experiments still requires extensive spin dynamical simulations for a fully quantitative analysis.

Analogous experiments may be applied in isotropic solution, where the higher order multiple-quantum excitation is somewhat easier (*46*). In this case, the geometric information is provided through the cross-correlated relaxation of multiple-quantum coherence. 2Q-HLF experiments of this kind have already proven to be very useful (*47, 48*). Higher order cross-correlated relaxation experiments should also be feasible.

ACKNOWLEDGMENTS

This research was supported by the Swedish Natural Science Foundation and the Göran Gustafsson Foundation for Research in the Natural Sciences and Medicine. A.B. has been supported by a Marie Curie Research Training Grant from the European Union. We thank O. G. Johannessen for technical assistance.

REFERENCES

1. M. H. Levitt, D. P. Raleigh, F. Creuzet, and R. G. Griffin, Theory and simulations of homonuclear spin pair systems in rotating solids, *J. Chem. Phys.* **90,** 6347–6364 (1990).
2. T. Gullion and J. Schaefer, Detection of weak heteronuclear dipolar coupling by rotational-echo double-resonance nuclear magnetic resonance, *Adv. Magn. Reson.* **13,** 57–83 (1989).
3. Y. Ishii, T. Terao, and M. Kainosho, Relayed anisotropy correlation NMR: Determination of dihedral angles in solids, *Chem. Phys. Lett.* **265,** 133–140 (1996).
4. K. Schmidt-Rohr, Torsion angle determination in solid ^{13}C-labelled amino acids by SLF 2Q-NMR, *J. Am. Chem. Soc.* **118,** 7601–7603 (1996).
5. D. P. Weliky and R. Tycko, Determination of peptide conformations by 2D MAS NMR exchange spectroscopy with rotor synchronization, *J. Am. Chem. Soc.* **118,** 8487–8488 (1996).
6. X. Feng, Y. K. Lee, D. Sandström, M. Edén, H. Maisel, A. Sebald, and M. H. Levitt, Direct determination of a molecular torsional angle by solid-state NMR, *Chem. Phys. Lett.* **257,** 314–320 (1996).
7. X. Feng, M. Edén, A. Brinkmann, H. Luthman, L. Eriksson, A. Gräslund, O. N. Antzutkin, and M. H. Levitt, Direct determination of a peptide torsional angle ψ by double-quantum solid-state NMR, *J. Am. Chem. Soc.* **119,** 12,006–12,007 (1997).
8. P. R. Costa, J. D. Gross, M. Hong, and R. G. Griffin, Solid-state NMR measurement of ψ in peptides: A NCCN 2Q-heteronuclear local field experiment, *Chem. Phys. Lett.* **280,** 95–103 (1997).
9. M. Hong, J. D. Gross, and R. G. Griffin, Site-resolved determination of peptide torsion angle ϕ from the relative orientations of backbone N–H and C–H bonds by solid-state NMR, *J. Phys. Chem. B* **101,** 5869–5874 (1997).
10. K. Schmidt-Rohr, A double-quantum solid-state NMR technique for determining torsion angles in polymers, *Macromolecules* **29,** 3975–3981 (1996).
11. Y. Tomita, E. J. O'Connor, and A. E. McDermott, A method for dihedral angle measurement in solids: Rotational resonance NMR of a transition-state inhibitor of triose phosphate isomerase, *J. Am. Chem. Soc.* **116,** 8766–8771 (1994).
12. X. Feng, P. J. E. Verdegem, Y. K. Lee, D. Sandström, M. Edén, P. Bovee-Guerts, W. J. de Grip, J. Lugtenburg, H. J. M. de Groot, and M. H. Levitt, Direct determination of a molecular torsional angle in the membrane protein rhodopsin by solid-state NMR, *J. Am. Chem. Soc.* **119,** 6853–6857 (1997).
13. J. Schaefer, REDOR-determined distances from heterospins to clusters of ^{13}C labels, *J. Magn. Reson.* **137,** 272–275 (1999).
14. T. Gullion and C. H. Pennington, θ-REDOR: An MAS NMR method to simplify multiple coupled heteronuclear spin systems, *Chem. Phys. Lett.* **290,** 88–93 (1998).
15. D. P. Weitekamp, J. R. Garbow, and A. Pines, Determination of dipole coupling constants using heteronuclear multiple quantum NMR, *J. Chem. Phys.* **77,** 2870–2883 (1982).
16. B. H. Meier and W. L. Earl, Excitation of multiple quantum transitions under magic angle spinning conditions: Adamantane, *J. Chem. Phys.* **85,** 4905–4911 (1986).
17. Y. Ba and W. S. Veeman, On multiple quantum NMR of coupled spins in solids, *Isr. J. Chem.* **32,** 173–178 (1992).
18. Y. Ba and W. S. Veeman, Experimental detection of multiple-quantum coherence transfer in coupled spin solids by multi-dimensional NMR experiments, *Solid State NMR* **2,** 131–141 (1993).
19. J. Gottwald, D. E. Demco, R. Graf, and H. W. Spiess, High-resolution double-quantum NMR spectroscopy of homonuclear spin pairs and proton connectivities in solids, *Chem. Phys. Lett.* **243,** 314–323 (1995).
20. H. Geen, J. J. Titman, J. Gottwald, and H. W. Spiess, Solid-state proton multiple-quantum NMR spectroscopy with fast magic angle spinning, *Chem. Phys. Lett.* **227,** 79–86 (1994).
21. U. Friedrich, I. Schnell, D. E. Demco, and H. W. Spiess, Triple-

quantum NMR spectroscopy in dipolar solids, *Chem. Phys. Lett.* **285,** 49–58 (1998).

22. H. Geen, R. Graf, A. S. D. Heindrichs, B. S. Hickman, I. Schnell, H. W. Spiess, and J. J. Titman, Spin counting with fast MAS, *J. Magn. Reson.* **138,** 167–172 (1999).
23. B. E. Scruggs and K. K. Gleason, Multiple-quantum NMR coherence growth in polycrystalline salts containing ^{19}F, *J. Magn. Reson.* **99,** 149–160 (1992).
24. O. N. Antzutkin and R. Tycko, High-order multiple quantum excitation in ^{13}C nuclear magnetic resonance spectroscopy of organic solids, *J. Chem. Phys.* **110,** 2749–2752 (1999).
25. K. K. Gleason, Creating multiple-quantum coherences in solids, *Concepts Magn. Reson.* **5,** 199–216 (1993).
26. A. E. Bennett, R. G. Griffin, and S. Vega, Recoupling of homo- and heteronuclear dipolar interactions in rotating solids, *NMR Basic Principles and Progress* **33,** 1–77 (1994).
27. S. Dusold and A. Sebald, Dipolar recoupling under magic-angle-spinning conditions, *Ann. Rep. NMR Spectrosc.* **41,** 185–264 (2000).
28. D. M. Gregory, M. A. Metha, J. C. Shiels, and G. P. Drobny, Determination of local structure in solid nucleic acids using double quantum nuclear magnetic resonance spectroscopy, *J. Chem. Phys.* **107,** 28–42 (1997).
29. M. Edén and M. H. Levitt, Excitation of carbon-13 triple quantum coherence in magic-angle-spinning NMR, *Chem. Phys. Lett.* **293,** 173–179 (1998).
30. G. Metz, X. Wu, and S. O. Smith, Ramped-amplitude cross polarization in magic-angle-spinning NMR, *J. Magn. Reson. A* **110,** 219–227 (1994).
31. M. Hohwy, H. J. Jakobsen, M. Edén, M. H. Levitt, and N. C. Nielsen, Broadband dipolar recoupling in the nuclear magnetic resonance of rotating solids: A compensated C7 pulse sequence, *J. Chem. Phys.* **108,** 2686–2694 (1998).
32. Y. K. Lee, N. D. Kurur, M. Helmle, O. G. Johannessen, N. C. Nielsen, and M. H. Levitt, Efficient dipolar recoupling in the NMR of rotating solids. A sevenfold symmetric radiofrequency pulse sequence, *Chem. Phys. Lett.* **242,** 304–309 (1995).
33. M. Edén and M. H. Levitt, Pulse sequence symmetries in the nuclear magnetic resonance of spinning solids: Application to heteronuclear decoupling, *J. Chem. Phys.* **111,** 1511–1519 (1999).
34. A. Brinkmann, M. Edén, and M. H. Levitt, Synchronous helical pulse sequences in magic-angle-spinning NMR. Double quantum spectroscopy of recoupled multiple-spin systems, *J. Chem. Phys.,* in press.
35. A. Brinkmann, M. Edén, and M. H. Levitt, Double-quantum magic-angle-spinning NMR. Phase timing relationships and the compensation of chemical and Bloch-Siegert shifts, unpublished manuscript (1999).
36. M. Munowitz, A. Pines, and M. Mehring, Multiple-quantum dynamics in NMR: A directed walk through Liouville space, *J. Chem. Phys.* **86,** 3172–3182 (1987).
37. R. Tycko, Selection rules for multiple quantum NMR experiments in solids: Derivation from time-reversal symmetry and comparison with simulations and ^{13}C NMR experiments, *J. Magn. Reson.* **139,** 302–307 (1999).
38. M. Carravetta, M. Edén, X. Zhao, A. Brinkmann, and M. H. Levitt, Symmetry principles for the design of radiofrequency pulse sequences in the nuclear magnetic resonance of rotating solids, *Chem. Phys. Lett.,* in press.
39. T. Gullion, D. B. Baker, and M. S. Conradi, New, compensated Carr-Purcell sequences, *J. Magn. Reson.* **89,** 479–484 (1990).
40. R. R. Ernst, G. Bodenhausen, and A. Wokaun, "Principles of Nuclear Magnetic Resonance in One and Two Dimensions," Clarendon Press, Oxford (1987).
41. D. A. Varshalovich, A. N. Moskalev, and V. K. Khersonskii, "Quantum Theory of Angular Momentum," World Scientific, Singapore (1988).
42. J. Jeener, Superoperators in magnetic resonance, *Adv. Magn. Reson.* **10,** 1 (1982).
43. M. Hohwy, C. M. Rienstra, C. P. Jaroniec, and R. G. Griffin, Fivefold symmetric homonuclear dipolar recoupling in rotating solids: Application to double quantum spectroscopy, *J. Chem. Phys.* **110,** 7983–7992 (1999).
44. V. Lalitha, E. Subramanian, and J. Bordner, Structure and conformation of linear peptides: Part IV—Crystal structure of L-Alanyl-glycyl-glycine monohydrate, *Ind. J. Pure Appl. Phys.* **23,** 506–508 (1985).
45. K. Nomura, K. Takegoshi, T. Terao, K. Uchida, and M. Kainosho, Determination of the complete structure of a uniformly labelled molecule by rotational resonance solid-state NMR in the tilted rotating frame, *J. Am. Chem. Soc.* **121,** 4064–4065 (1999).
46. M. H. Levitt and R. R. Ernst, Multiple-quantum excitation and spin topology filtration in high-resolution NMR, *J. Chem. Phys.* **83,** 3297–3310 (1985).
47. B. Reif, M. Hennig, and C. Griesinger, Direct measurement of angles between bond vectors in high-resolution NMR, *Science* **276,** 1230–1233 (1997).
48. S. Ravindranathan, X. Feng, T. Karlsson, G. Widmalm, and M. H. Levitt, Investigation of carbohydrate conformation in solution and in powders by double-quantum NMR, *J. Am. Chem. Soc.* **122,** 1102–1115 (2000).